THE ASTRONOMICAL JOURNAL, 120:2670–2678, 2000 November

A MORPHOLOGICAL DIAGNOSTIC FOR DYNAMICAL EVOLUTION OF WOLF-RAYET BUBBLES

ROBERT A. GRUENDL, YOU-HUA CHU, BRYAN C. DUNNE, AND SEAN D. POINTS[1]
Department of Astronomy, University of Illinois, 1002 West Green Street, Urbana, IL 61801; gruendl@astro.uiuc.edu, chu@astro.uiuc.edu, carolan@astro.uiuc.edu, points@astro.uiuc.edu
Received 2000 July 3; accepted 2000 July 19

ABSTRACT

We have observed Hα and [O III] emission from eight of the most well-defined Wolf-Rayet ring nebulae in the Galaxy. We find that in many cases the outermost edge of the [O III] emission leads the Hα emission. We suggest that these offsets, when present, are due to the shock from the Wolf-Rayet bubble expanding into the circumstellar envelope. Thus, the details of the WR bubble morphology at Hα and [O III] can then be used to understand better the physical condition and evolutionary stage of the nebulae around Wolf-Rayet stars, as well as to place constraints on the nature of the stellar progenitor and its mass-loss history.
Key words: circumstellar matter — ISM: bubbles — stars: Wolf-Rayet

1. INTRODUCTION

Ring nebulae around Wolf-Rayet (WR) stars were first reported by Johnson & Hogg (1965). The first three WR rings reported, NGC 2359, NGC 6888, and S 308 (Sharpless 1959), all show an indisputable shell morphology. Since then many more ring nebulae have been identified in the Galaxy (Chu 1981; Heckathorn, Bruhweiler, & Gull 1982; Miller & Chu 1993; Marston, Chu, & García-Segura 1994a; Marston et al. 1994b) and in the Magellanic Clouds (Chu & Lasker 1980; Dopita et al. 1994). A wide range of morphology is observed in these WR ring nebulae, but most of these nebulae do not have a distinct ring morphology as did the first three identified. While a small number of the WR ring nebulae may be misidentifications, in which the WR stars are not responsible for the nebular morphology, the majority of them may represent the cumulative product of interactions between the ambient interstellar medium (ISM) and the stellar winds since the star was formed.

To explain the wide range of morphology observed in WR rings, analytic models and numerical simulations have been put forward for windblown bubbles in different media: in a homogeneous ISM (e.g., Weaver et al. 1977), in a cloudy ISM (McKee, van Buren, & Lazareff 1984), and in a circumstellar medium (García-Segura & Mac Low 1995a, 1995b). The most sophisticated models for WR ring nebulae have been presented by García-Segura, Langer, & Mac Low (1996a) and García-Segura, Mac Low, & Langer (1996b), who have taken into account the evolution and mass-loss history over the lifetime of the central star. These models show that an interstellar bubble is formed around a massive star during its main-sequence lifetime, and subsequently a circumstellar bubble will be formed interior to the interstellar bubble after the star has made a transition from a red supergiant (RSG) or luminous blue variable (LBV) to a WR star. They further predict that evolved circumstellar bubbles will fragment and form break-out regions where the shock fronts (as traced by [O III] emission) lead the fragmented circumstellar shell material (traced by Hα and [N II] emission).

The models of García-Segura et al. (1996a, 1996b) are successful in explaining the morphology and chemical abundances of NGC 6888 and S 308, but it is difficult to generalize this success to more WR rings for two reasons. First, most of the WR ring nebulae have nondistinctive ring morphology, and hence their physical nature is uncertain and comparisons with models can produce ambiguous results at best. Second, most WR ring nebulae do not have detailed follow-up observations of morphology, kinematic properties, or chemical abundances for comparison with models.

To study the structure and evolution of ring nebulae around WR stars and to compare them with those of García-Segura et al. models (1996a, 1996b), we have selected a set of WR nebulae that have the best-defined, most distinct shell morphology. These are the WR nebulae that have the most nearly complete kinematic and abundance information available, and they are the most likely to yield meaningful results. We have imaged these WR rings in Hα and [O III] λ5007 emission and used the nebular morphology in these two spectral lines to study the physical structure of these nebulae. We have examined their physical structures in conjunction with the chemical abundances, kinematic properties, and sizes of the shells and with the spectral type of the WR stars. This examination is supported by comparison with models of WR ring evolution. The results are reported in this paper. In § 2, we describe the observations. In § 3, we describe individual objects, and in § 4, we discuss the physical significance of the [O III] and Hα morphologies and compare the observed nebular morphologies with models and discuss their evolutionary stages.

2. OBSERVATIONS AND DATA REDUCTION

The observations were obtained with the 1 m telescope at the Mount Laguna Observatory (MLO) and the Curtis Schmidt Telescope at Cerro Tololo Inter-American Observatory (CTIO) in several observing runs. The journal of observations is given in Table 1.

The MLO 1 m observations were made with two substantially different detectors and narrowband filter sets. Observations made before 1992 used a Texas Instruments 800×800 CCD as a detector and used a focal reducer. The resulting images have 0″.98 pixels and cover a 13′.1 field of

[1] Visiting astronomer, Cerro Tololo Inter-American Observatory, National Optical Astronomy Observatories, operated by the Association of Universities for Research in Astronomy, Inc., under a cooperative agreement with the National Science Foundation.

TABLE 1

Observation Summary

Telescope	Date	Filter (Å)[a]	Exposure (s)	Resolution (arcsec)
NGC 2359:				
MLO 1 m	1999 Oct	6563/20	1800	3.5
MLO 1 m	1999 Oct	5015/49	1800	4.0
G2.4+1.4:				
MLO 1 m	1991 Jul	6567/62	600	3.3
MLO 1 m	1991 Jul	5015/49	600	3.3
WR 128:				
MLO 1 m	1999 Jul	6563/20	1200	3.0
MLO 1 m	1999 Jul	5015/49	1200	2.3
WR 134:				
MLO 1 m	1991 Jul	6567/62	600	2.9
MLO 1 m	1991 Jul	5015/49	600	3.0
NGC 6888:				
MLO 1 m	1991 Jul	6567/62	300	3.1
MLO 1 m	1991 Jul	5015/49	900	3.6
S 308:				
MLO 1 m	1999 Jan	6563/20	1200	3.5
MLO 1 m	1999 Jan	6563/20	1200	3.4
RCW 58:				
Curtis-Schmidt......	1996 Dec	6568/30	900	3.8
Curtis-Schmidt......	1996 Dec	5023/40	1800	3.4
RCW 104:				
Curtis-Schmidt......	1992 Jun	6563/14	600	2.6
Curtis-Schmidt......	1992 Jun	5007/44	600	2.9

[a] Values are given as central wavelength per FWHM.

view. The typical seeing was $\sim 2''$ when these images were taken, but the focal reducer degraded the image quality at the edge of the field to $\sim 4''$. The Hα filter used had central wavelength 6567 Å and FWHM 62 Å and thus also transmitted the [N II] λλ6548, 6584 lines. The [O III] observations were made with a filter centered at 5015 Å with FWHM 49 Å, which isolated the [O III] λ5007 line.

The observations made after 1992 at MLO used a Loral 2k × 2k CCD. Here the individual frames have a 13.′6 field of view with 0.″4 pixel^{-1} scale. Typical seeing during the observations was between 1.″5 and 2.″0. The filter used for the Hα observations has FWHM 20 Å centered at 6563 Å, which should isolate the Hα line from most emission of the nearby [N II] λλ6548, 6584 lines. The [O III] filter had FWHM 50 Å centered at 5010 Å.

Observations of RCW 104 were obtained with the CTIO Curtis Schmidt telescope on 1992 June 29. A Thompson 1k × 1k CCD detector was used with a 31′ field of view and 1.″84 pixel^{-1} scale. The filter used for the Hα observation had FWHM 17 Å centered at 6563 Å, while the [O III] filter had FWHM 44 Å centered 5007 Å. The observations of RCW 58 were also obtained with the Curtis Schmidt telescope at CTIO on 1996 December 31. These observations used a Tektronics 2k × 2k CCD detector with a 69′ field of view and 2.″03 pixel^{-1} scale. The filter used for the Hα observations was centered at 6568 Å with FWHM 30 Å, while the [O III] filter had FWHM 40 Å centered at 5023 Å.

The observations of NGC 6888, S 308, WR 128, and WR 134 required multiple fields to cover the entire nebula (or in the case of S 308 to cover a portion of the object). The individual frames have been combined into a single mosaic for each object. Each frame was registered to adjacent frames by using the stars in the region of overlap between frames. Furthermore, the observing conditions often varied substantially over the course of the observations. The offset due to changing sky background for the frames in each mosaic image was removed using the method outlined in Regan & Gruendl (1995). For each final image or mosaic an astrometric solution was found by comparison with stellar positions in the Guide Star Catalog 1.2 (Roser et al. 1998). The absolute positional accuracy for each image is better than 0.″4. More important for this work, the relative positional accuracy of the Hα and [O III] images is estimated from the stellar images. In this case the typical uncertainty in the registration between the Hα and [O III] images has been reduced to less than 0.1 pixels.

3. RESULTS

We detect Hα and [O III] emission from all eight WR nebulae. In Figures 1 through 8, we present the Hα and [O III] images of these WR ring nebulae. In addition to the emission-line images of each nebula, we present an [O III] to Hα ratio image to show the relative positions of [O III] and Hα emission. Note that the ratios are relative rather than absolute because most of the observations were made during nonphotometric conditions. In the [O III]/Hα ratio images, strong Hα emission (relative to [O III]) appears dark (*black*), while regions where [O III] emission is comparatively bright appear light (*white*).

The ratio maps in panels (*c*) in Figs. 1 through 8 help highlight the locations where the Hα and [O III] morphology show spatial differences. In many cases the ratio maps clearly demonstrate that the outer edge of the WR bubble as seen in [O III] emission (the [O III] front) is exterior to the edge of the bubble as traced by Hα emission (the Hα front). Careful examination of the Hα and [O III] images shows four types of relationships between the Hα and [O III] fronts:

Type I morphology has no measurable offset between the Hα and [O III] fronts. This type includes NGC 2359 and G2.4+1.4.

Type II morphology has an Hα front trailing closely behind an [O III] front, and both fronts have a similar shape. Examples of this type include WR 128, WR 134, S 308, and parts of NGC 6888 (the caps along the major axis).

Type III morphology has bright Hα emission trailing far behind a faint [O III] front. In this type, the Hα appearance can differ significantly from the [O III] appearance, for example, RCW 58.

Type IV morphology has a faint [O III] front with no Hα counterpart. For example, RCW 104 and parts of NGC 6888 (along the minor axis).

In Table 2 we present the physical parameters measured, along with values taken from the literature. There we include the spectral type of the WR star, distance, WR wind velocity and mass-loss rate, WR bubble radius as measured from the [O III] image, WR bubble expansion velocity, dynamical timescale ($\equiv$Radius/$V_{\rm exp}$), the typical angular and linear offset between Hα and [O III] emission, the type of offsets observed, nebular abundances, and galactocentric distance.

3.1. *Description of Individual Nebulae*

3.1.1. *S 308 (WR 6)*

S 308, around the WN5 star HD 50896, is the closest WR ring nebula that has been identified. The low surface bright-

TABLE 2

Observed and Measured Parameters

Quantity[a]	NGC 2359	G2.4+1.4	WR 128	WR 134	NGC 6888	RCW 58	RCW 104	S 308
Spectral type	WN4	WO1	WN4	WN6	WN6	WN8	WN5	WN5
Distance (kpc)	3.5	4.0	4.0	2.1	1.8	4.0	4.0	1.6
V_∞ (km s^{-1})	...	...	2270	1905	1605	975	...	1720
log $\dot{M}$ ($M_\odot$ yr^{-1})	...	...	...	-4.13	-4.02	...	...	-4.12
Radius (pc)	2.1	2.7	6.2	6.6	4.5	5.7	5.9	9.0
V_{exp} (km s^{-1})	18	42	...	>50	80	110	...	65
Dyn. timescale (10^4 yr)	11.3	8.8	...	<10.7	5.5	5.1	...	13.5
Typical offset (arcsec)	<1.5	<1	3–5	4–8	10	18–40	3.0	16–20
Typical offset (pc)	<0.025	<0.03	0.06–0.10	0.04–0.08	0.09	0.35–0.78	0.06	0.12–0.17
Offset type	I	I	II	II	II, IV	III	II, IV	II
12 + log O/H	8.24	8.45	...	8.83	8.14	8.72	8.48	8.03
log N/O	-0.95	-0.49	...	-0.85	$+0.27$	-0.30	-0.13	$+0.22$
Y	0.3	0.47	...	0.31	0.29	0.43	0.31	0.45
Gal. distance (kpc)	15	7	7	10	10	10	8	11

[a] Distance and galactocentric distance are from van der Hucht et al. (1988). Stellar wind V_∞ and log ($\dot{M}$) are from Prinja, Barlow, & Howarth (1990). Radius is measured from the [O III] image. Expansion velocities are from the following: NGC 2359, WR 134, and NGC 6888, Treffers & Chu (1982); G2.4+1.4, Dopita & Lozinskaya (1990); RCW 58, Chu (1988); S 308, Chu et al. (1982). Abundance measurements are from Esteban et al. (1992). Local ISM abundances: 12 + log O/H = 8.7, log N/O = -1.12, $Y = 0.285$.

ness and large angular diameter, $\sim 40'$, of this nebula make imaging the entire structure difficult. Figure 1 shows the northwest and western limbs, which are also the brightest portion of the bubble. A large Type II offset between the [O III] and Hα emission is clearly visible along the northern and western rims of S 308. A dramatic break-out structure is evident in the northwest corner (best seen in the [O III] image, Fig. 1*b*).

3.1.2. *NGC 2359* (*WR 7*)

The WR bubble in NGC 2359 (see Fig. 2) is associated with the WN4 star HD 56925. The [O III]/Hα ratio image shows no offset between the tracers (a Type I morphology) along the main shell structure, similar to the ratio maps shown by Dufour (1994). In addition to the WR bubble, there also appears a second, larger, parabolic arc of emission, which shares its eastern boundary with the WR ring nebula. This arc of material is bounded by an H II region to the south and molecular material to the east and south (Schneps et al. 1981; Gruendl & Chu 2000).

3.1.3. *RCW 58* (*WR 40*)

RCW 58 (see Fig. 3) is associated with the WN8 star HD 96548 (WR 40). In Hα emission the bubble appears to be composed primarily of radial filaments, while the fainter [O III] emission appears smoother and significantly more extended (Type III morphology). The extended [O III] morphology was originally noted by Chu (1982) and is one of

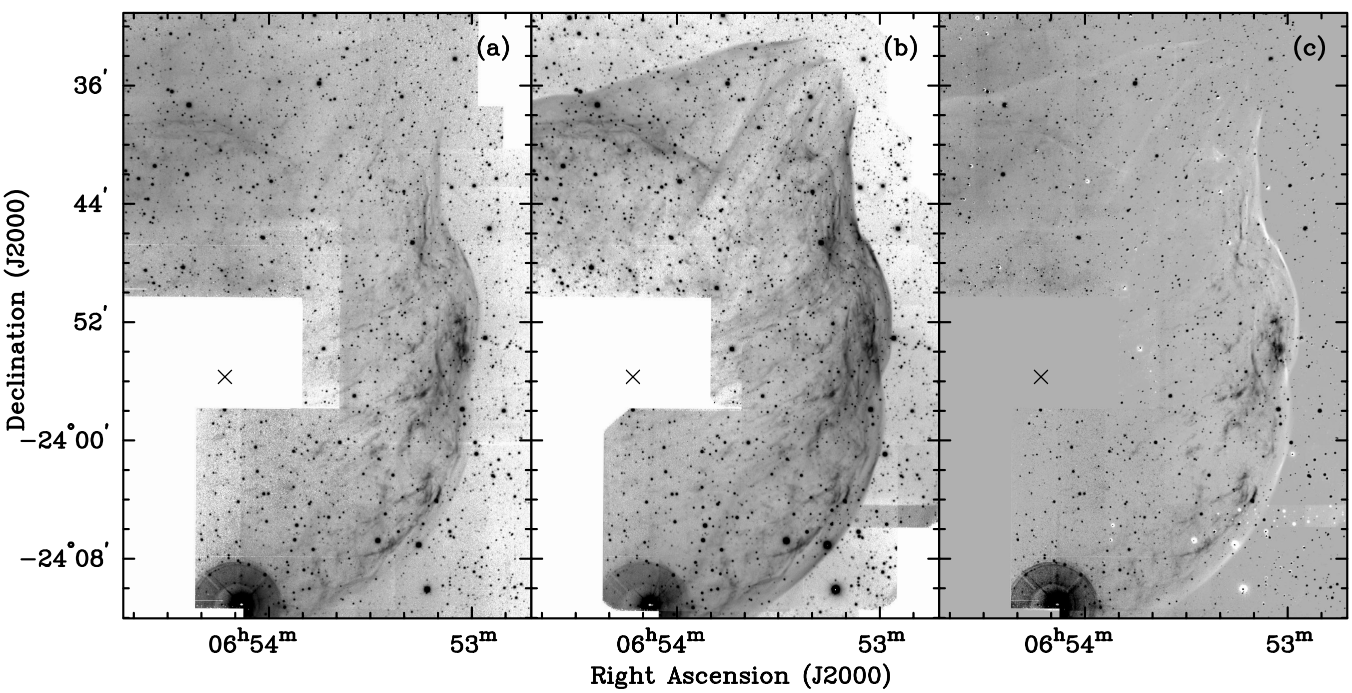

Fig. 1.—Images of S 308: (*a*) Hα emission, (*b*) [O III] emission for the same field of view as (*a*), and (*c*) composite of Hα (*black*) and [O III] (*white*) emission. For more details about the composite image, see § 3. A cross marks the WR star associated with the nebulosity in each image.

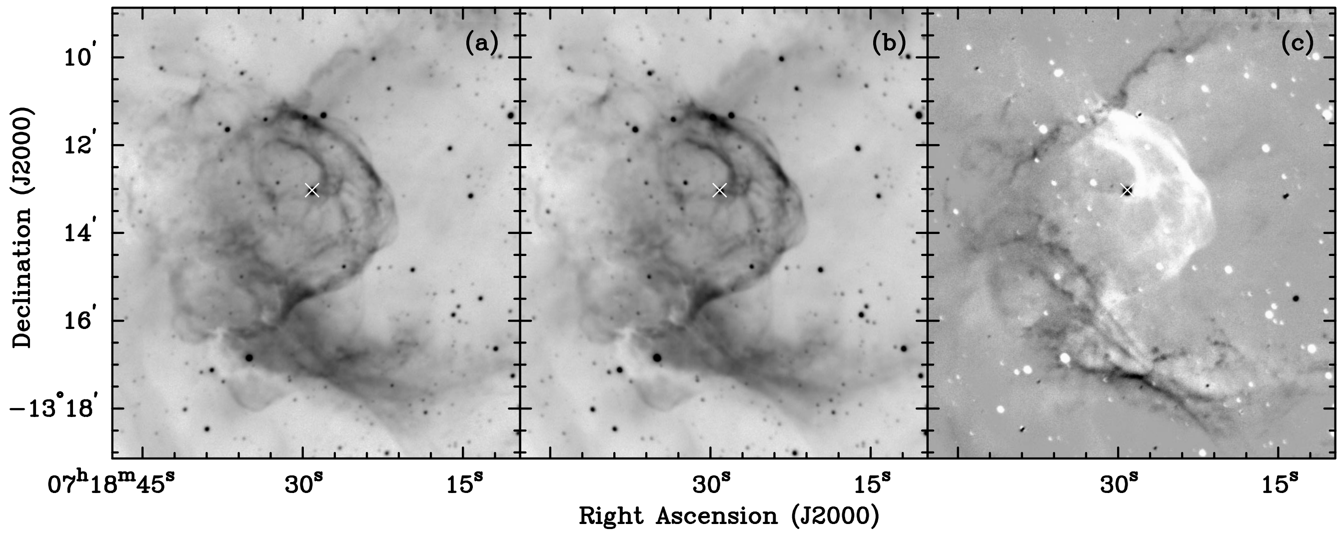

FIG. 2.—Same as Fig. 1, but for NGC 2359

the clearest offsets between the Hα and [O III] emission in our sample. Part of the extended [O III] emission on the eastern limb appears to form a concave bulge significantly different from Hα morphology that may be a pronounced break-out structure.

3.1.4. *RCW 104* (*WR 75*)

RCW 104 (see Fig. 4) was originally identified by Smith (1967) around the WN5 star HD 147419 (WR 75). Because of complex filamentary Hα emission on the same sight line, the Hα emission associated with the WR star is not clearly defined except on the western limb. The [O III] emission has a limb-brightened, barrel-shaped appearance that is composed of tangential filaments on the eastern and western limbs. The southwestern limb is the only location where both Hα and [O III] emission are observed. At this location, there appears to be a slight Type II offset of the [O III] emission exterior to the Hα limb. The entire eastern limb shows no Hα counterpart and therefore is classified as Type IV morphology. In the southwestern corner the [O III] emission has a faint structure similar in character to the break-out structure in RCW 58 and S 308.

3.1.5. *G2.4+1.4* (*WR 102*)

G2.4 + 1.4 (see Fig. 5) is another ring nebulae in our sample that has no discernible offset between [O III] and Hα (Type I morphology). Among the WR stars in our sample, WR 102, or LSS 4368, is the only WO star. The field around WR 102 is highly confused by interstellar emission along the same sight line. Dopita & Lozinskaya (1990) have made extensive kinematic observations and suggested that the bubble is a " blister " structure on the front of a dense cloud.

3.1.6. *Anon* (*WR 128*)

Previous Hα and [O III] images of nebulosity associated with WR 128 have concentrated on the two prominent arcs to the north and east of the central WN4 star, HD 187282. There are no published emission line images that extend an equal distance to the south and west to determine whether the partial ring has other components. We have imaged an

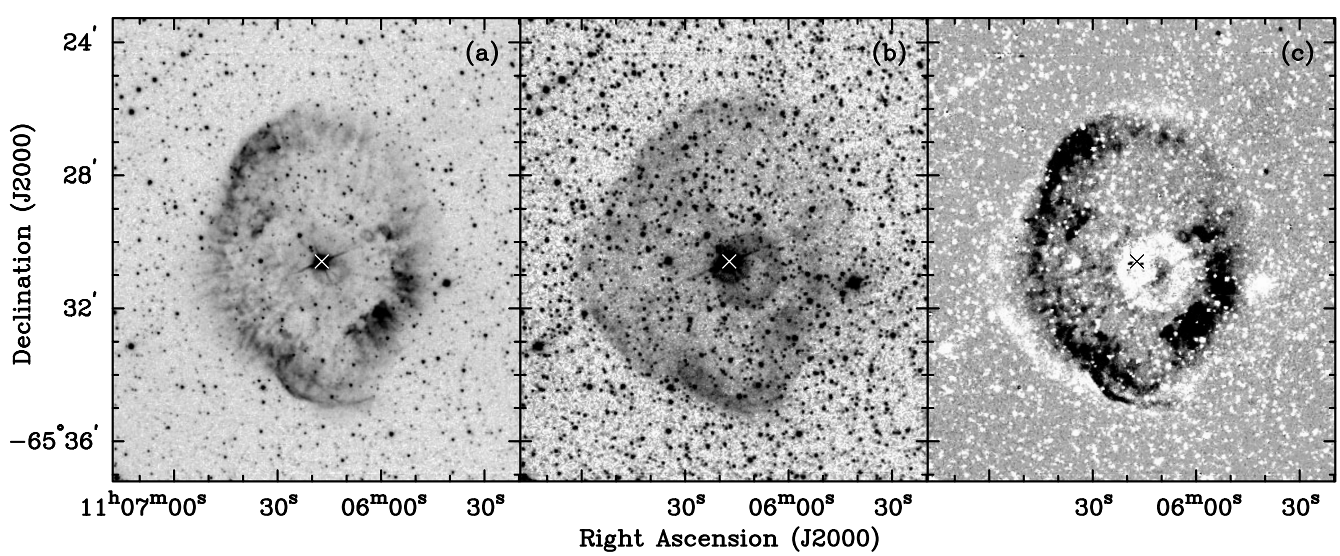

FIG. 3.—Same as Fig. 1, but for RCW 58

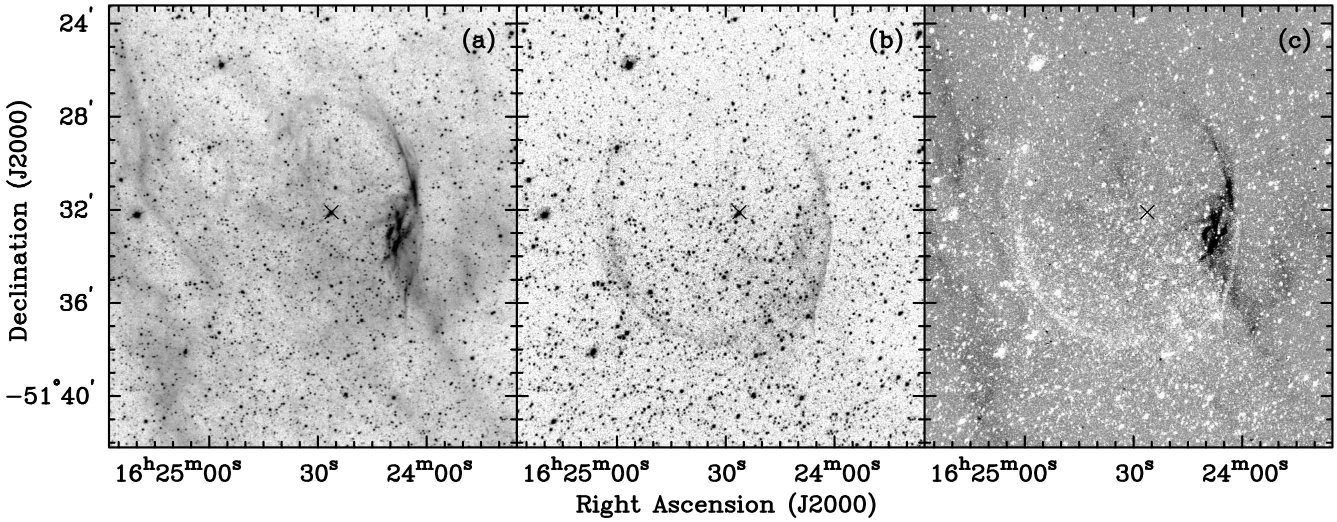

FIG. 4.—Same as Fig. 1, but for RCW 104

area that extends as far south and west as to the north and east and confirm that there is no bright Hα or [O III] emission on the opposite side of HD 187282. Our images (Fig. 6) do show that the arc east of HD 187282 continues farther south than previously known (Miller & Chu 1993). The composite image (Fig. 6*c*) shows that the [O III] emission is significantly offset exterior from the Hα emission with respect to the central star (Type II morphology). Recent H I observations by Arnal et al. (1999) show that there is an H I hole coincident with WR 128. In the Hα image the arc of "limb-brightened" emission appears to be "filled" with low surface brightness emission from the shell to roughly the position of the WR star.

3.1.7. *Anon* (*WR 134*)

WR 134 (see Fig. 7) is the WN6 star HD 191765. The nebular images show markedly different morphology in Hα and [O III]. The Hα image shows a hemisphere of filamentary emission, along with nonuniform diffuse Hα emission. The [O III] emission is all filamentary and is present only to the northwest of HD 191765. Much of the Hα emission southwest of the WR star has been shown by Treffers & Chu (1982) to be kinematically distinct from the filamentary emission. The [O III] filaments appear slightly offset radially outward with respect to the Hα filaments (Type II morphology). The WR star is projected close to the center of the filamentary emission. In the composite image, offsets between the filaments in Hα and [O III] are not very clear, in part due to the large dynamic range in the Hα image. The outermost [O III] filaments are similar in morphology to the break-out features observed in NGC 6888.

3.1.8. *NGC 6888* (*WR 136*)

NGC 6888 around the WN6 star HD 192163 is often regarded as the prototypical WR bubble. The Hα and [O III] images (see Fig. 8) show a clear offset between the Hα and [O III] emission along the limb-brightened shell. Furthermore, a faint network of filamentary structures appears to envelop the Hα emission (Type II morphology). Beside the filamentary structures near the Hα emission, there is a large [O III] front with no Hα counterpart that bulges outward from the northwest limb of the bubble near the minor axis (Type IV morphology). This was previously noted by Miller & Chu (1993) and by Dufour (1994). In

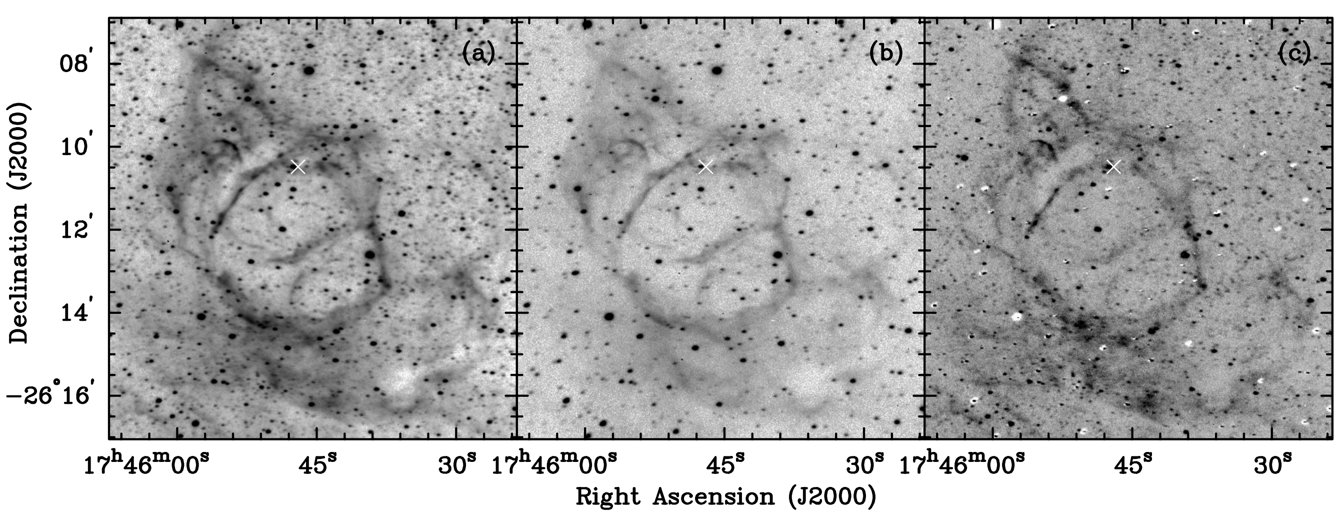

FIG. 5.—Same as Fig. 1, but for G2.4 + 1.4

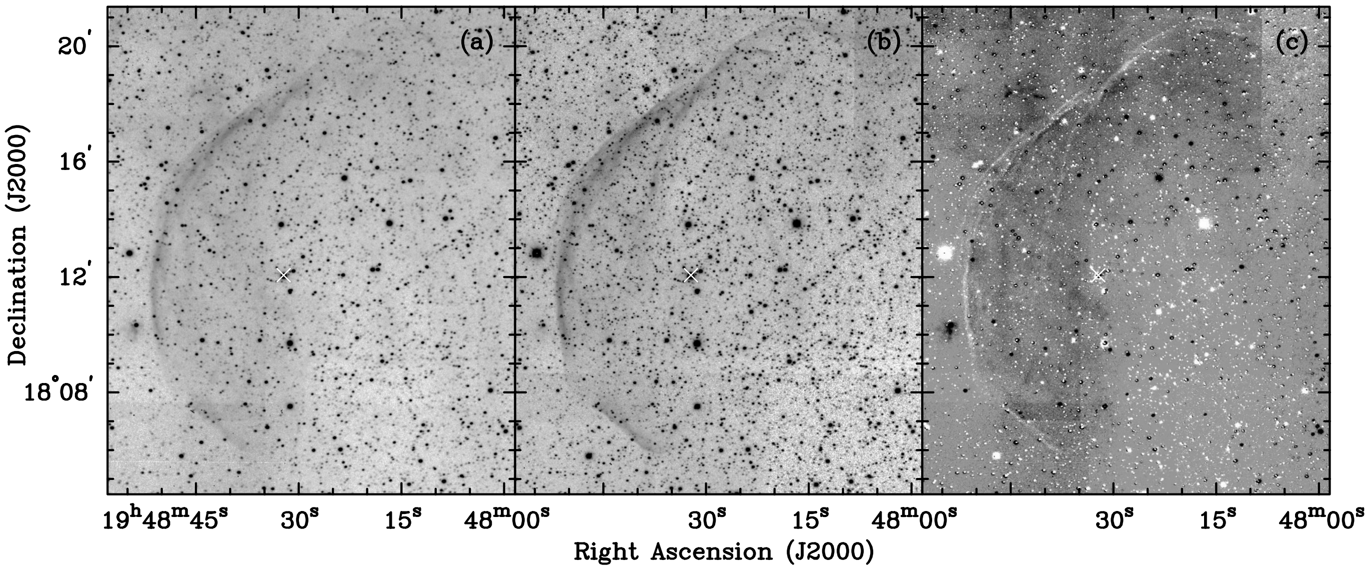

FIG. 6.—Same as Fig. 1, but for WR 128

Figure 8*c* it is apparent that the total extent of the [O III] emission is centered on the WR star, while the limb-brightened Hα shell is off-center. High-resolution *Hubble Space Telescope* Wide Field Planetary Camera 2 images of a portion of the shell rim presented by Moore, Hester, & Scowen (2000) show the offsets along the shell rim with dramatic clarity.

4. DISCUSSION

4.1. *Physical Significance of* Hα *and* [O III] *Morphologies*

Hα and [O III] line images of a nebula provide useful diagnostics of its physical structure. Hα is a recombination line and thus shows the overall distribution of ionized material, but because the line strength of Hα decreases with temperature its sensitivity drops for temperatures greater than 10^4 K. On the other hand, the [O III] line originates in a forbidden transition whose upper level is populated by collisional excitation; therefore its intensity increases with temperature, and [O III] line images trace high-excitation regions with temperatures $\geq 10^4$ K. Consequently, we expect the Hα and [O III] morphologies to be different, especially over regions where physical conditions change rapidly.

Behind a shock front, radiative cooling takes place; as the temperature drops, the density increases. Thus, a displacement between [O III] emission and Hα emission occurs (Cox 1972). The magnitude of the displacement depends on the postshock temperature, which is determined by the shock velocity, and the cooling rate, which is dependent on the density and metallicity. In cases in which a shock propagates into a dense medium, the cooling rate behind the shock front is high, the cooling zone is narrow, and the offset between Hα and [O III] emission peaks is minimal. For a shock propagating in a tenuous medium, the cooling rate is lower, the cooling zone is wider, and thus the offset between the Hα and [O III] emission peaks is larger and may be observable. If the ambient density is low enough, it

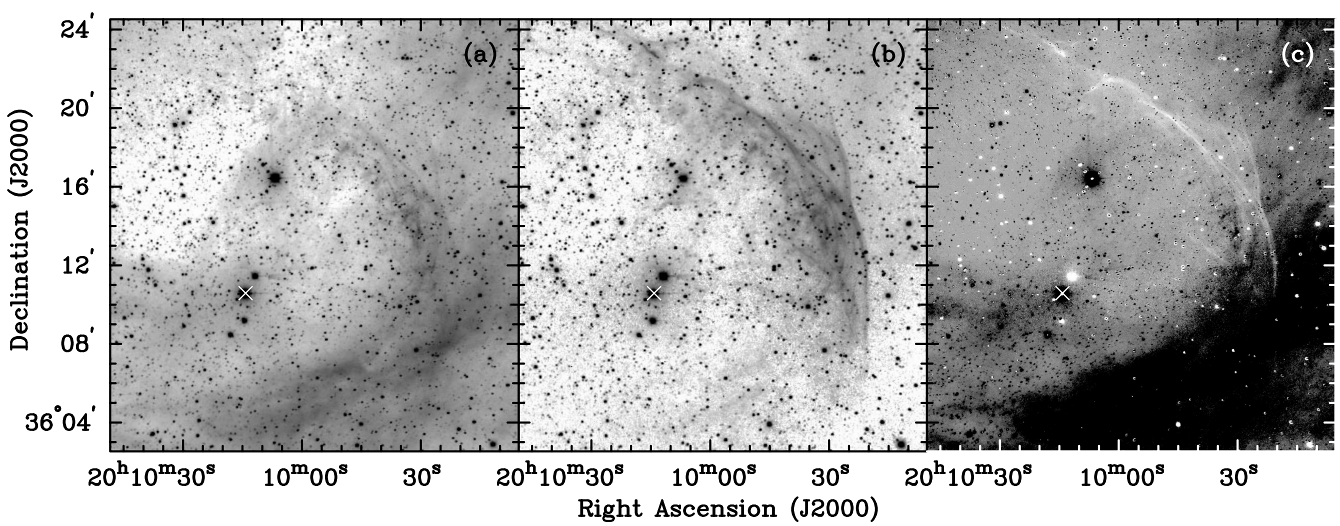

FIG. 7.—Same as Fig. 1, but for WR 134

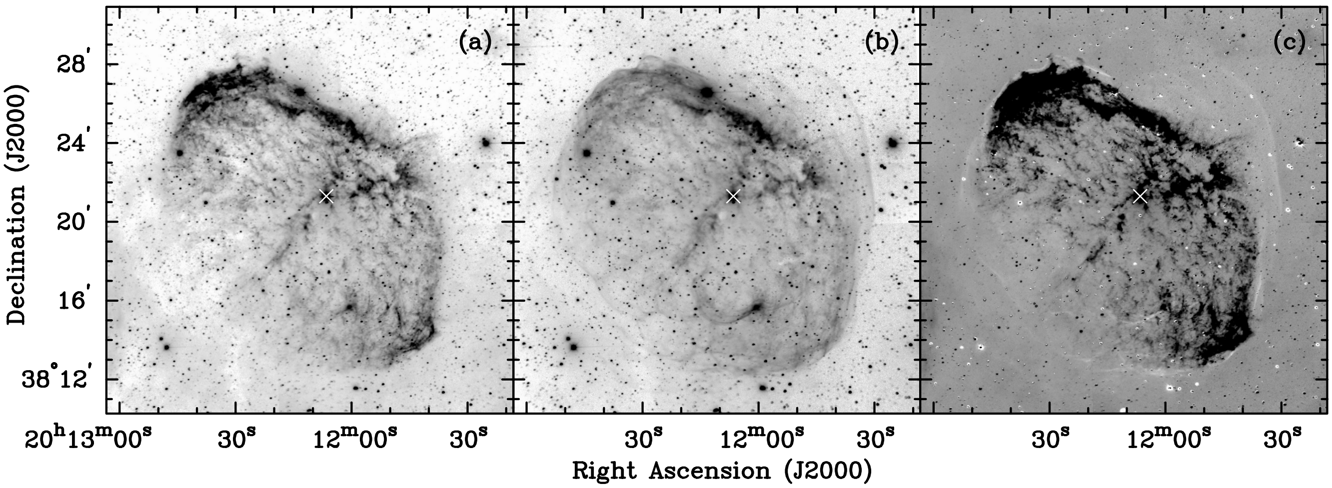

FIG. 8.—Same as Fig. 1, but for NGC 6888

is possible that [O III] emission is observable behind the shock, while Hα emission is too faint to be detected. Finally, if a shock propagates through a high-density medium and then into a low-density medium, it is possible to see bright Hα emission associated with the dense medium and a leading [O III] front associated with the recently shocked low-density medium. This could produce the largest displacement between the leading edges of Hα and [O III] emission.

Cox (1972) has calculated the expected one-dimensional surface brightness profile for Hβ and [O III], assuming a planar shock propagating at 100 km s^{-1} into a medium of density 1 cm^{-3} (see Fig. 3 in Cox 1972). This calculation found the separation between the peak Hβ and [O III] emission to be roughly 0.001 pc. For a WR star that had a RSG progenitor, its WR bubble will be expanding into a circumstellar envelope whose density can be calculated from the RSG wind properties. For a RSG mass-loss rate of 10^{-5} $M_\odot$ yr^{-1} and wind velocity 50 km s^{-1}, the RSG wind density at 6 pc from the star would be ~ 0.02 cm^{-3}. If we assume that the shock from the WR bubble is expanding into the circumstellar envelope (RSG wind) at 100 km s^{-1}, then the postshock density would be ~ 50 times lower and the cooling timescale ~ 50 times longer than Cox's results. Thus, the separation between Hα (or Hβ) and [O III] would be ~ 50 times greater, or ~ 0.05 pc. This order-of-magnitude estimate is similar to the typical observed separation between Hα and [O III] fronts in our sample (see Table 2).

The four types of relationship between the Hα and [O III] fronts described in § 3 can all be interpreted as shocks propagating into different ambient media. WR bubbles with the Type I Hα and [O III] fronts may be expanding into dense media; the cooling rate is high, and the displacement between Hα and [O III] emission peaks cannot be resolved by our images. WR bubbles with Type II Hα and [O III] fronts are probably expanding into a medium with density low enough that the cooling time behind the shock is long, and therefore an observable displacement between the [O III] and Hα fronts is produced. Type III Hα and [O III] fronts can be produced if a shock has propagated through a dense medium into a tenuous medium. The Hα morphology is determined by the dense medium, while the [O III] emission traces the progression of the shock in the tenuous medium. WR bubbles with Type IV morphology are expanding into a very tenuous medium. The postshock density is low and temperature is high, so that only [O III] emission, but not Hα, is strong enough to be detected.

4.2. *Comparison with Predictions of Theoretical Models*

García-Segura et al. (1996a, 1996b) have simulated the hydrodynamical evolution of circumstellar gas around a massive star, taking into account the stellar evolution and mass-loss history starting from the main sequence through the WR phase. WR stars can be descendants of either LBV or RSG progenitors; accordingly, García-Segura et al. have simulated nebulae around a 60 $M_\odot$ star that has gone through an LBV phase and a 35 $M_\odot$ star that has gone through a RSG phase. These simulations produce WR bubbles with distinctly different morphologies, kinematics, and abundances. These predictions, when compared with observations, can be used to determine the evolutionary stage of the WR bubble and the nature of the WR progenitor.

For a 60 $M_\odot$ star, García-Segura et al. (1996b) predict that the resulting WR bubble will be observable only in the early WR stage. After the WR bubble has swept up most of the LBV wind material, it will expand into a low-density circumstellar medium. This drop in the ambient density causes an increase in the shock velocity and the fragmentation of the dense WR shell. Thus, the resultant observable WR bubble will have a radial filamentary Hα structure in the dense shell and will be surrounded by [O III] emission behind the accelerating outer shock in the tenuous circumstellar medium. This fits precisely the Type III Hα and [O III] morphology observed in WR bubbles. Indeed García-Segura et al. (1996b) have suggested that RCW 58 was produced this way and that its central star is a descendant of a star that went through an LBV phase.

For 35 $M_\odot$ stars, García-Segura et al. (1996a) have performed calculations for those with RSG wind velocities of 15 and 75 km s^{-1}. For the case of a 75 km s^{-1} RSG wind velocity, they predict that the swept-up WR shell is dense enough to be observable only during the early stages, when the radius is ≤ 1 pc. For the case of a RSG with a slow wind, ~ 15 km s^{-1}, their model shows that the outer edge of the RSG wind is compressed into a RSG shell and the inner edge is swept up by WR wind into a WR shell. The WR shell collides with the outer RSG shell after $\sim 10^4$ yr, leading to a deceleration and brightening of the WR shell. After the collision, the dense clumps in the WR shell, having higher inertia, cross the RSG shell and form blowouts. Eventually, the whole bubble fragments and the shocked WR wind breaks out and forms an outer shock leading the fragmented WR shell.

Note that these models can be used only qualitatively, as many approximations and simplifications have been made. We note particularly that the physical distinction between the models using 15 and 75 km s^{-1} RSG wind is really in the density of the RSG wind, which is proportional to $\dot{M}/V$, where $\dot{M}$ is the mass-loss rate of the RSG and V is the RSG wind velocity. Therefore, the model of García-Segura et al. (1996a) for the slow RSG wind is applicable for a faster RSG wind with a larger RSG mass-loss rate.

The model of García-Segura et al. (1996a, 1996b) for a low-density RSG wind (low $\dot{M}/V$) produces WR bubbles that have thick shells when they are dense enough to be observable in Hα and [O III]. None of the WR bubbles we observe fit this description. On the other hand, their model for a high-density RSG wind (high $\dot{M}/V$) produces WR bubbles with thin shells that are most observable when the WR shell collides with the RSG shell. Within 1000–2000 yr after the collision, the thin shell expands into a tenuous circumstellar medium and its [O III] emission should lead the Hα emission, similar to the Type II morphology. After the WR shell fragments and breakouts occur, the outer shocks may be observable in [O III] but not in Hα, producing a Type IV morphology.

García-Segura et al. (1996a, 1996b) suggested that NGC 6888 was produced by a WR star that went through its RSG phase with a slow wind velocity and S 308 was produced with a faster RSG wind velocity. Our images support their interpretation that NGC 6888 had a denser RSG wind than S 308. S 308 must be near the stage in which the WR shell has collided with the RSG shell. The thickness and break-out structure of the S 308 shell are more consistent with the predictions of their slow RSG wind model (high $\dot{M}/V$). We suggest that NGC 6888, S 308, WR 128, WR 134, and RCW 104 all have RSG progenitors and that the RSG wind of NGC 6888 was significantly denser than the others.[2]

[2] Abundance measurements show enrichment of CNO processed elements in NGC 6888, S 308, and RCW 104, which demonstrates the circumstellar origin of the bubble material. The abundance measurements of the nebula around WR 134 were made in the diffuse Hα arc (Esteban et al. 1992), which is kinematically different from the [O III] bubble and has been identified as an H II region (Treffers & Chu 1982). Future abundance measurements need to be made for the nebula around WR 128 and the [O III] filaments around WR 134 to confirm their circumstellar origin.

Finally, two WR bubbles in our sample do not resemble any of the bubble morphologies expected in the models of García-Segura et al. (1996a, 1996b). These two bubbles, NGC 2359 and G2.4+1.4, show no offsets between the Hα and [O III] fronts. These two objects are also the smallest and have the slowest expansion velocities. When compared with the other WR bubbles in our sample, their dynamical timescales are long (old) for their size. These results may be explained by their interstellar environment, which is denser than what García-Segura et al. (1996a, 1996b) have assumed. NGC 2359, being adjacent to molecular clouds, is clearly in a denser interstellar environment. Consequently, the interstellar bubble blown by the progenitor over its main-sequence lifetime is small and dense, and the circumstellar bubble of the WR star can easily merge with this interstellar bubble. The bubble in NGC 2359 is dominated by swept-up interstellar material, as indicated by the abundances measured (Esteban et al. 1992). The situation for G2.4+1.4 is less certain because of its confusing line of sight near the Galactic center (Dopita & Lozinskaya 1990).

4.3. *Future Work*

The analysis presented in this paper has been unavoidably qualitative. A number of observations are needed to understand better the physical state of circumstellar material around WR stars so that a quantitative assessment can be made. Because of the low density in the bubbles, flux-calibrated narrowband imaging in the Hα line would yield detailed surface brightness profiles of the gas and allow us to derive the rms density of the bubble. High-dispersion spectroscopic observations of Hα and [O III] would show the relative expansion velocity of shock fronts in each tracer and should verify our interpretation of Type III and IV morphologies. Furthermore, these observations would provide a detailed snapshot of the kinematics of filaments and knots in the fragmenting shell that might identify the instabilities responsible for their formation. Detailed abundance measurements within the shock fronts, filaments, and knots will probe not only the chemical composition but also the nucleosynthetic yields and mixing as a massive star evolves. Finally, sensitive X-ray observations with new instruments such as *XMM Newton* would probe the shocked fast wind that drives the nebular expansion. These observations could probe the mass-loss history of the central star, pinpoint the nature of the progenitor, and make a detailed assessment of the physical processes that occur in bubble formation.

R. A. G. is supported by the NASA grant SAO GO 0-1004X. The use and operation of the Mount Laguna Observatory are supported by the Department of Astronomy at the University of Illinois and the Department of Astronomy at San Diego State University.

REFERENCES

Arnal, E. M., Cappa, C. E., Rizzo, J. R., & Cichowolski, S. 1999, AJ, 118, 1798
Chu, Y.-H. 1981, ApJ, 249, 195
———. 1982, ApJ, 254, 578
———. 1988, PASP, 100, 986
Chu, Y.-H., Gull, T. R., Treffers, R. R., Kwitter, K. B., & Troland, T. H. 1982, ApJ, 254, 562
Chu, Y.-H., & Lasker, B. M. 1980, PASP, 92, 730
Cox, D. P. 1972, ApJ, 178, 143
Dopita, M. A., Bell, J. F., Chu, Y.-H., & Lozinskaya, T. A. 1994, ApJS, 93, 455
Dopita, M. A., & Lozinskaya, T. A. 1990, ApJ, 359, 419
Dufour, R. J. 1994, in Circumstellar Media in Late Stages of Stellar Evolution, ed. R. E. S. Clegg, I. R. Stevens, & W. P. S. Meikle (Cambridge: Cambridge Univ. Press), 78
Esteban, C., Vilchez, J. M., Smith, L. J., & Clegg, R. E. S. 1992, A&A, 259, 629
García-Segura, G., Langer, N., & Mac Low, M.-M. 1996a, A&A, 316, 133
García-Segura, G., & Mac Low, M.-M. 1995a, ApJ, 455, 145
———. 1995b, ApJ, 455, 160
García-Segura, G., Mac Low, M.-M., & Langer, N. 1996b, A&A, 305, 229
Gruendl, R. A., & Chu, Y.-H. 2000, in preparation
Heckathorn, J. N., Bruhweiler, F. C., & Gull, T. R. 1982, ApJ, 252, 230
Johnson, H. M., & Hogg, D. E. 1965, ApJ, 142, 1033
Marston, A. P., Chu, Y.-H., & García-Segura, G. 1994a, ApJS, 93, 229
Marston, A. P., Yocum, D. R., García-Segura, G., & Chu, Y.-H. 1994b, ApJS, 95, 151
McKee, C. F., van Buren, D., & Lazareff, B. 1984, ApJ, 278, L115
Miller, G. J., & Chu, Y.-H. 1993, ApJS, 85, 137
Moore, B. D., Hester, J. J., & Scowen, P. A. 2000, AJ, 119, 2991
Prinja, R. K., Barlow, M. J., & Howarth, I. D. 1990, ApJ, 361, 607
Regan, M. W., & Gruendl, R. A. 1995, in ASP Conf. Ser. 77, Astronomical Data Analysis Software and Systems IV, ed. R. A. Shaw, H. E., Payne, & J. J. E. Hayes (San Francisco: ASP), 335
Roser, S., Morrison, J. E., Bucciarelli, B., Lasker, B., & McLean, B. J. 1998, in IAU Symp. 179, New Horizons from Multi-wavelength Sky Surveys, ed. B. J. McLean, D. A. Golombek, J. J. E. Hayes, & H. E. Payne (Dordrecht: Kluwer), 420
Schneps, M. H., Hascheck, A. D., Wright, E. L., & Barrett, A. H. 1981, ApJ, 243, 184
Sharpless, S. 1959, ApJS, 4, 257
Smith, L. J. 1967, Ph.D. thesis, Australian National Univ.
Treffers, R. R., & Chu, Y.-H. 1982, ApJ, 254, 569
van der Hucht, K. A., Hidayat, B., Admiranto, A. G., Supelli, K. R., & Doom, C. 1988, A&A, 199, 217
Weaver, R., McCray, R., Castor, J., Shapiro, P., & Moore, R. 1977, ApJ, 218, 377